

Article

# Carbon Dioxide Conversion with High-Performance Photocatalysis into Methanol on NiSe<sub>2</sub>/WSe<sub>2</sub>

Zheng Luo <sup>1,†</sup>, Yinghan Li <sup>1,†</sup> , Fengbo Guo <sup>2,\*</sup> , Kaizhi Zhang <sup>2</sup>, Kankan Liu <sup>2</sup>, Wanli Jia <sup>2</sup>, Yuxia Zhao <sup>2</sup> and Yan Sun <sup>2</sup>

<sup>1</sup> Department of Civil and Environmental Engineering, University of Washington, Seattle, WA 98195, USA; luozheng@uw.edu (Z.L.); yinghl2@uw.edu (Y.L.)

<sup>2</sup> School of Environment and Safety Engineering, North University of China, Taiyuan 030051, China; s12345yadc@163.com (K.Z.); liukk@nuc.edu.cn (K.L.); jiauly15@nuc.edu.cn (W.J.); zhaoyuxia1000@163.com (Y.Z.); sunyan30000@163.com (Y.S.)

\* Correspondence: gfbo@nuc.edu.cn

† These authors contributed equally to this work.

Received: 21 July 2020; Accepted: 18 August 2020; Published: 21 August 2020



**Abstract:** Climate change has been recognized as a threatening environmental problem around the world. CO<sub>2</sub> is considered to be the main component of greenhouse gas. By using solar energy (light energy) as the energy source, photocatalytic conversion is one of the most effective technologies to reveal the clean utilization of CO<sub>2</sub>. Herein, using sodium tungstate, nickel nitrate, and selenium powder as the main raw materials, the high absorption and utilization of WSe<sub>2</sub> for light energy and the high intrinsic conductivity of NiSe<sub>2</sub> were combined by a hydrothermal method to prepare NiSe<sub>2</sub>/WSe<sub>2</sub> and hydrazine hydrate as the reductant. Then, high-performance NiSe<sub>2</sub>/WSe<sub>2</sub> photocatalytic material was prepared. The characterization results of XRD, XPS, SEM, specific surface area, and UV-visible spectroscopy show that the main diffraction peak of synthesized NiSe<sub>2</sub>/WSe<sub>2</sub> is sharp, which basically coincides with the standard card. After doping NiSe<sub>2</sub>, the morphology of WSe<sub>2</sub> was changed from a flake shape to smaller and more trivial crystal flakes, which demonstrates richer exposed edges and more active sites; the specific surface area increased from 3.01 m<sup>2</sup> g<sup>-1</sup> to 8.52 m<sup>2</sup> g<sup>-1</sup>, and the band gap becomes wider, increasing from 1.66 eV to 1.68 eV. The results of a photocatalytic experiment show that when the prepared NiSe<sub>2</sub>/WSe<sub>2</sub> catalyst is used to conduct photocatalytic reduction of CO<sub>2</sub>, the yield of CH<sub>3</sub>OH is significantly increased. After reaction for 10 h, the maximum yield could reach 3.80 mmol g<sup>-1</sup>, which presents great photocatalytic activity.

**Keywords:** NiSe<sub>2</sub>/WSe<sub>2</sub>; photocatalysis; CO<sub>2</sub>; methanol

## 1. Introduction

CO<sub>2</sub>, whose primary resource is the combustion of fossil fuel and the massive emission of automobiles, is currently ongoing excessive emission. It is the main cause of the greenhouse effect [1–3]. An effective measure to address the greenhouse effect is to convert the CO<sub>2</sub> in air into organic chemical fuel. Photocatalytic technology has attracted great attention due to its mild conditions, environmental friendliness, effectiveness, no secondary pollution, and other advantages. However, current catalysts have various shortages, such as less-specific surface-active sites, a fast recombination rate of photoelectron–hole pair, low quantum efficiency, and a low absorption and utilization rate of sunlight. Therefore, searching for effective catalysts has become the focus of researchers around the world [4–6].

In recent years, transition metal nitride [7], transition metal carbide [8], and transition metal chalcogenide [9] have all presented the characteristics of low cost and great catalytic stability.

Among them, the two-dimensional layered transition metal chalcogenide (TDMC)  $\text{MX}_2$  (M represents the transition metal element, and X represents S, Se, and Te) has the characteristic of changing from an indirect band gap to a direct band gap during the transition from multiple layers to a single layer [10,11]. At present, there is much research on the preparation and performance of  $\text{MoS}_2$  and its composite materials, but research on  $\text{WSe}_2$  compounded with other metal ions has been little studied [12,13]. As the main transition metal chalcogenide, tungsten diselenide ( $\text{WSe}_2$ ) is a diamagnetic *p*-type semiconductor material, which locates at a low conduction band (1.16 eV).  $\text{WSe}_2$  is the material with the lowest thermal conductivity in the world, which indicates that the heat will not be easily dissipated from the system; in other words, the efficiency needed for the system to convert energy will be higher [14]. Therefore, the application of this new material with high energy efficiency can be regarded as a significant improvement. Furthermore, when  $\text{WSe}_2$  changes from bulk material to a single-layer material, its energy gap will vary with the change of layers. At a single layer, the electronic structure will experience significant change, and the 1.2 eV indirect band gap will suddenly change into a 1.8 eV direct band gap. Such a band gap width is very close to the solar spectrum, so  $\text{WSe}_2$  has high optical adsorption properties and exhibits great application prospects in the fields of photoelectrocatalysis and photoelectric conversion [15]. Besides,  $\text{WSe}_2$  exhibits dose-dependent toxicological effects compared with other similar inorganic analogues such as  $\text{MoS}_2$  or  $\text{WS}_2$  [16]. This character denotes that the hazardous level of this component is relatively low. The two-dimensional layered transition metal chalcogenides generally have the problems of poor electrical conductivity, a tendency for aggregation, and difficulty in preparing several layers [17], which has severely affected their catalytic performance. In order to address these problems, the researchers have conducted significant investigations. Yu et al. [18] synthesized reduced graphene oxide (RGO) onto the single-layer  $\text{WSe}_2$  nanolayer via the one-pot solvothermal reaction. They found that compared with the bare  $\text{WSe}_2$  nanosheets, the composite material synthesized with RGO has higher photocatalytic activity. Similarly, Wang et al. [19] employed the same method to prepare the multi-walled carbon-nanotubes-modified  $\text{WSe}_2$  (CNT/ $\text{WSe}_2$ ). Based on analysis of their research conclusion, it can be found that when exposed to visible light, the CNT/ $\text{WSe}_2$  composite material shows increased photocatalytic activity during the photocatalytic decomposition of the organic dye methyl orange (MO). Furthermore, Stuart Licht et al. [20] pointed out that the cationic dissolving salt can affect the photoelectric properties of the  $\text{WSe}_2$  nanolayer. Moreover, Feng et al., Li et al., and Guo et al. [21–23] pointed out that the photopotential and photoelectrochemical cell power can be significantly enhanced when transition-metal chalcogenides were employed for electrodes, especially for  $\text{MoSe}_2$ /graphene and  $\text{WSe}_2$ /graphene nanosheets and core-shell structure of  $\text{NiSe}_2$  nanoparticles@nitrogen-doped graphene.

According to the reaction process of the photocatalytic reduction of  $\text{CO}_2$ ,  $\text{CO}_2$  must be attached to the active sites of the photocatalyst to further process a reaction, which is the basis of the interfacial reaction. Therefore, the enhancement of the photocatalytic reduction of  $\text{CO}_2$  reaction can start from the enhancement of carbon dioxide adsorption. In previous studies, a  $\text{TiO}_2$ -based heterostructured photocatalyst and *g*- $\text{C}_3\text{N}_4$ -based heterostructured photocatalyst were also applied to reduce  $\text{CO}_2$  to produce  $\text{CH}_3\text{OH}$  [24]. Yang et al. [25], Liang et al. [26], and Bafaqeer et al. [27] use *g*- $\text{C}_3\text{N}_4$ /CdS, *g*- $\text{C}_3\text{N}_4$ /ZnO,  $\text{ZnV}_2\text{O}_6$ /pCN as photocatalytic materials, and the methanol yields were  $1352.07 \text{ umol g}^{-1}$ ,  $0.6 \text{ mmol g}^{-1} \text{ h}^{-1}$ , and  $3742.19 \text{ umol gcat}^{-1}$ , respectively. Qin et al. [28] and Li et al. [29] use  $\text{CuO/TiO}_2$  and  $\text{BiS}_2/\text{TNT}$  as photocatalytic material to produce  $\text{CH}_3\text{OH}$ ; the yields of  $\text{CH}_3\text{OH}$  were  $1600 \text{ umol h}^{-1} \text{ g}^{-1}$  and  $224.6 \text{ umol}^{-1} \text{ g}^{-1} \text{ h}^{-1}$ , respectively. The results of the study show that carbon dioxide in the solution can be adsorbed on TDMCs to form formate ion. After 3 h of sunlight at room temperature, the system generates methanol photoelectrically. Further mechanism analysis shows that TDMC materials can not only adsorb and activate carbon dioxide but also contribute to the process of photogenerated electron transformation and act as a promoter [30].

In this work,  $\text{NiSe}_2/\text{WSe}_2$  was successfully prepared with a hydrothermal method. The main goal is to find a feasible way to catalyze the conversion of the  $\text{CO}_2$ . By doing so, this research intends to see to what extent the  $\text{CO}_2$  is converted. The overall situation ahead and afterwards, therefore,

has been compared. Besides, it is also worth figuring out whether the approach has the value to be promoted or not, say, if it is worthy and feasible enough to be considered as a regular way to treat the ongoing CO<sub>2</sub> emission problem. If so, the meaning of this research can thus be applied to a wider scope. Several different plans have been considered, while the choice of WSe<sub>2</sub>/NiSe<sub>2</sub> is due to the access to such material and its relatively high efficiency. The photocatalysis performance of WSe<sub>2</sub> by doping NiSe<sub>2</sub> to change WSe<sub>2</sub> morphology and electronic structure has been improved. Furthermore, its structure was characterized by adopting SEM, specific surface area (BET), XPS, and XRD, and its photocatalysis and CO<sub>2</sub> reducing property was also investigated.

## 2. Materials and Methods

### 2.1. Preparation of NiSe<sub>2</sub>/WSe<sub>2</sub>

The preparation method of the research is with the reference of Cao [31]. Specifically, 1.32 g sodium tungstate (Na<sub>2</sub>WO<sub>4</sub>·2H<sub>2</sub>O) and 0.58 g nickel nitrate were added in deionized (DI) water under stirring, and then the mixture was poured into the mixed solution containing 15 mL HCl solution and 10 mL hydrazine hydrate (N<sub>2</sub>H<sub>4</sub>·H<sub>2</sub>O) to obtain solution A. A total of 0.97 g of selenium powder was added to 15 mL hydrazine hydrate with a concentration of 80%, and then the resulting mixture underwent heating and a reflux reaction for 1–2 h to obtain the precursor B. After that, solution A was poured into precursor B, and ultrasonic treatment was conducted for the obtained mixture until solution A and precursor B were evenly mixed. Next, the mixture was performed on a 100 mL reaction kettle (reactor) and then experienced hydrothermal reaction for 48 h under 200 °C. After reaction and cooling, deionized water was employed to wash the resulting mixture 3–4 times, and then the obtained mixture was moved to the sodium hydroxide solution. Unreacted selenium powder was removed through a heating reaction, and then deionized water and ethyl alcohol were conducted to wash the mixture alternatively until the pH of the mixture was 7. The mixture was then moved into the 60 °C oven for drying. After drying, the mixture was placed into a tube furnace and then underwent reaction for 2–3 h under the condition of 500–550 °C in the nitrogen flow to obtain the NiSe<sub>2</sub>/WSe<sub>2</sub>. Figure 1 shows the block diagram of the preparation process of NiSe<sub>2</sub>/WSe<sub>2</sub>.

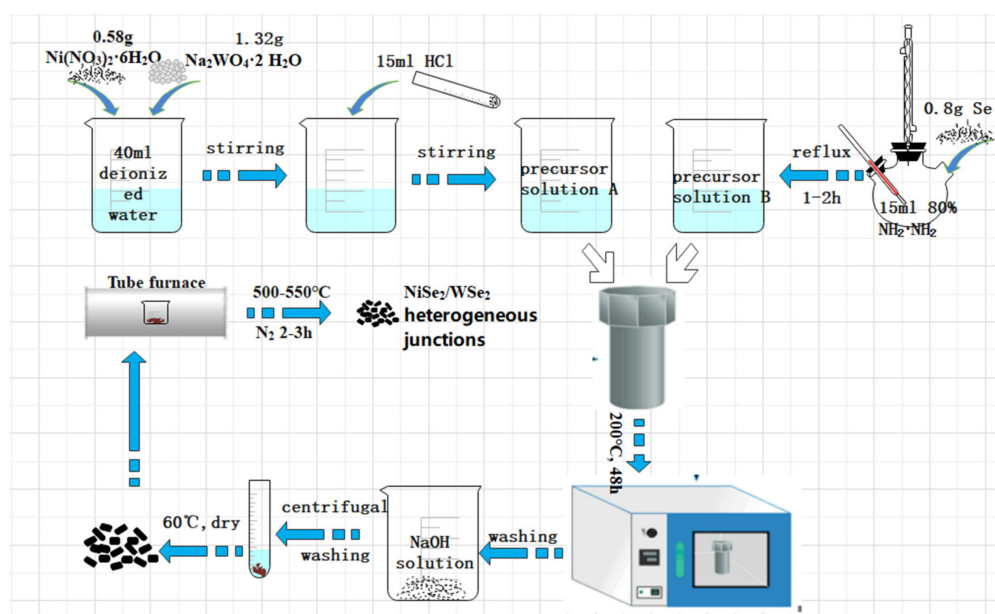


**Figure 1.** Block diagram of the preparation process of NiSe<sub>2</sub>/WSe<sub>2</sub>.

The process of WSe<sub>2</sub> preparation is almost identical to the description above, except for not adding the nickel nitrate.

## 2.2. Characterization

X-ray powder diffraction (XRD): The Japanese D/MaxRB X-ray Spectrometer was used (Cu target  $K\alpha$  ray) to test the chemical components of samples and their phase composition. The test double angle was  $2\theta = 10\text{--}80^\circ$ ; the UV-visible absorbance spectrum was tested using the ultraviolet-visible spectrophotometer (UV-Vis-8800S, Shanghai, China). The integrating sphere, whose function is to measure the absorbance of the powder sample, was applied in this section for the operation; the  $\text{BaSO}_4$  tablet was used to test the optical properties of sample, and the measurement range was 200–800 nm; the specific surface area (BET) test was conducted with the NOVA Touch 4LX instrument (Quantachrome Instruments, Boynton Beach, FL, U.S.), which can be used to test the specific surface area and pore size distribution; for the scanning electron microscope (SEM), we adopted the JSM-6700F field emission scanning electron microscope (resolution of 1.0 nm (15 KV)/2.2 nm (1 KV), with an accelerating voltage of 0.5–30 KV). X-ray photoelectron spectroscopy (XPS) was tested by using ThermoESCALAB250XI.

## 2.3. Photocatalytic Reduction Experiment of $\text{CO}_2$

The photocatalytic reduction of  $\text{CO}_2$ , as shown in Figure 2, is conducted in the photocatalytic reactor, which was produced by Beijing Newbet Technology Co., Ltd. (NBeT, Beijing, China). Six quartz tubes were prepared. A total of 50 mL of  $0.08 \text{ mol L}^{-1}$   $\text{NaHCO}_3$  solution and 50 mg of prepared catalyst were added into each quartz tube, and then magnetic stirring was conducted to evenly disperse the catalyst. Under dark conditions, we continuously injected  $\text{CO}_2$  for 30 min to remove air and complete the adsorption–desorption balance of  $\text{CO}_2$  by the catalyst; the 300W Xe light was used as the simulation light source. The photocatalysis reaction as conducted by filtering with the 420 nm filter, a 1 mL reaction solution was extracted every 2 h, and after removing the catalyst through centrifugation, gas chromatography (GC-920) was used to test the product content. The carrier gas of gas chromatography was high-purity  $\text{N}_2$ , the detector was a hydrogen flame ionization detector (FID), and the chromatographic column was a capillary column; the column temperature was  $120^\circ\text{C}$ , the inlet temperature was  $140^\circ\text{C}$ , and the detector temperature was  $160^\circ\text{C}$ .

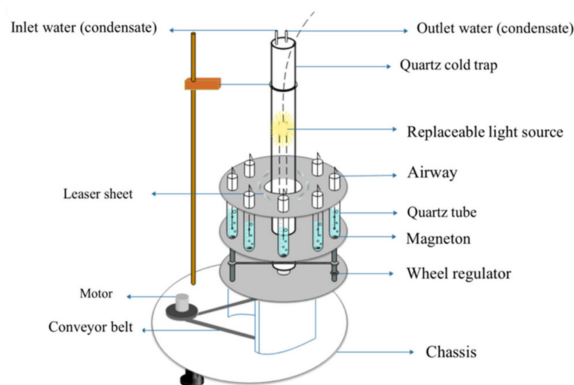


Figure 2. Reaction device for photocatalytic reduction of  $\text{CO}_2$ .

## 3. Results and Discussion

### 3.1. XRD and XPS Analysis

X-ray diffractograms of the synthesized  $\text{NiSe}_2/\text{WSe}_2$  were shown in Figure 3.

According to Figure 3, it can be seen that the main diffraction peak of synthesized  $\text{NiSe}_2/\text{WSe}_2$  presents a sharp peak value, and the positions of diffraction peaks basically coincide with the standard cards of  $\text{WSe}_2$  (JCPDS card, PDF#38–1388) and  $\text{NiSe}_2$  (JCPDS card, PDF#41–11495). Among them, the diffraction peaks at  $13.54^\circ$ ,  $31.69^\circ$ ,  $32.16^\circ$ ,  $34.21^\circ$ ,  $37.84^\circ$ ,  $47.39^\circ$ ,  $56.52^\circ$ , and  $57.92^\circ$  belong to the (002), (100), (101), (102), (103), (105), (008), and (112) crystal faces of  $\text{WSe}_2$ , respectively. Synthesized  $\text{WSe}_2$  diffraction peaks were also shown the same characteristics (Figure S1). The characterization

results are consistent with those of Jung [32]. The diffraction peaks at  $29.89^\circ$ ,  $33.41^\circ$ ,  $36.74^\circ$ ,  $45.37^\circ$ ,  $50.48^\circ$ ,  $57.57^\circ$ ,  $61.82^\circ$ ,  $64.01^\circ$ , and  $70.18^\circ$  belong to the (200), (210), (211), (221), (311), (321), (400), (410), and (420) crystal faces of  $\text{NiSe}_2$ , respectively. This indicates that the synthesized material is  $\text{NiSe}_2/\text{WSe}_2$  [33]. In order to further detect the composition and valence of surface elements, the XPS of  $\text{NiSe}_2/\text{WSe}_2$  spectrum was shown in Figure 4. Obviously, peaks of Ni, W, and Se were found in the full spectra. In the high-resolution spectra of  $\text{Ni}2p$ , its peak was composed of two peaks [34], where those at 872 eV and 875 eV were related to  $\text{Ni}2p_{1/2}$  and  $\text{Ni}2p_{2/3}$ , respectively. In the  $\text{Se}3d$  spectra, the peaks at 55.6 eV, 54.2 eV were assigned to the Se–Se, Ni–Se bonds. Three peaks positioned at 32.2 eV, 35.7 eV were ascribed to  $\text{W}4f_{5/2}$  and  $\text{W}4f_{7/2}$ . Similar results were obtained accordingly on the  $\text{W}4f$  and  $\text{Se}3d$  high-resolution spectra (Figure S2).

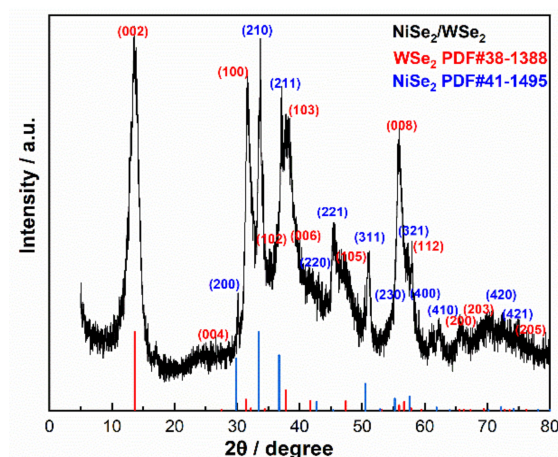


Figure 3. XRD of  $\text{NiSe}_2/\text{WSe}_2$ .

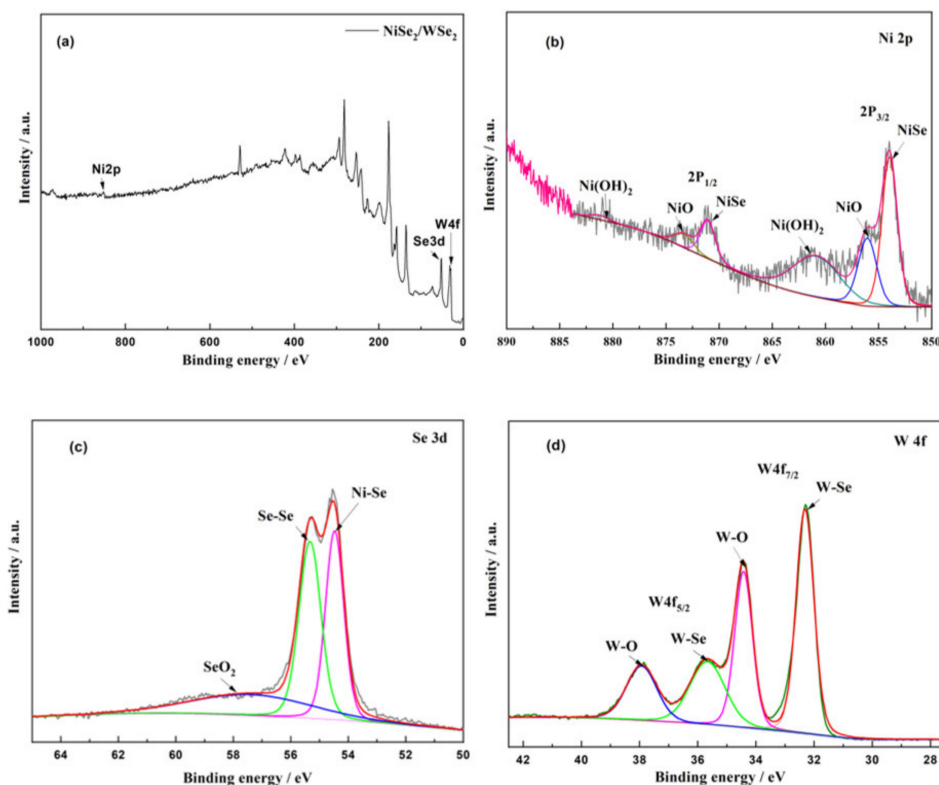
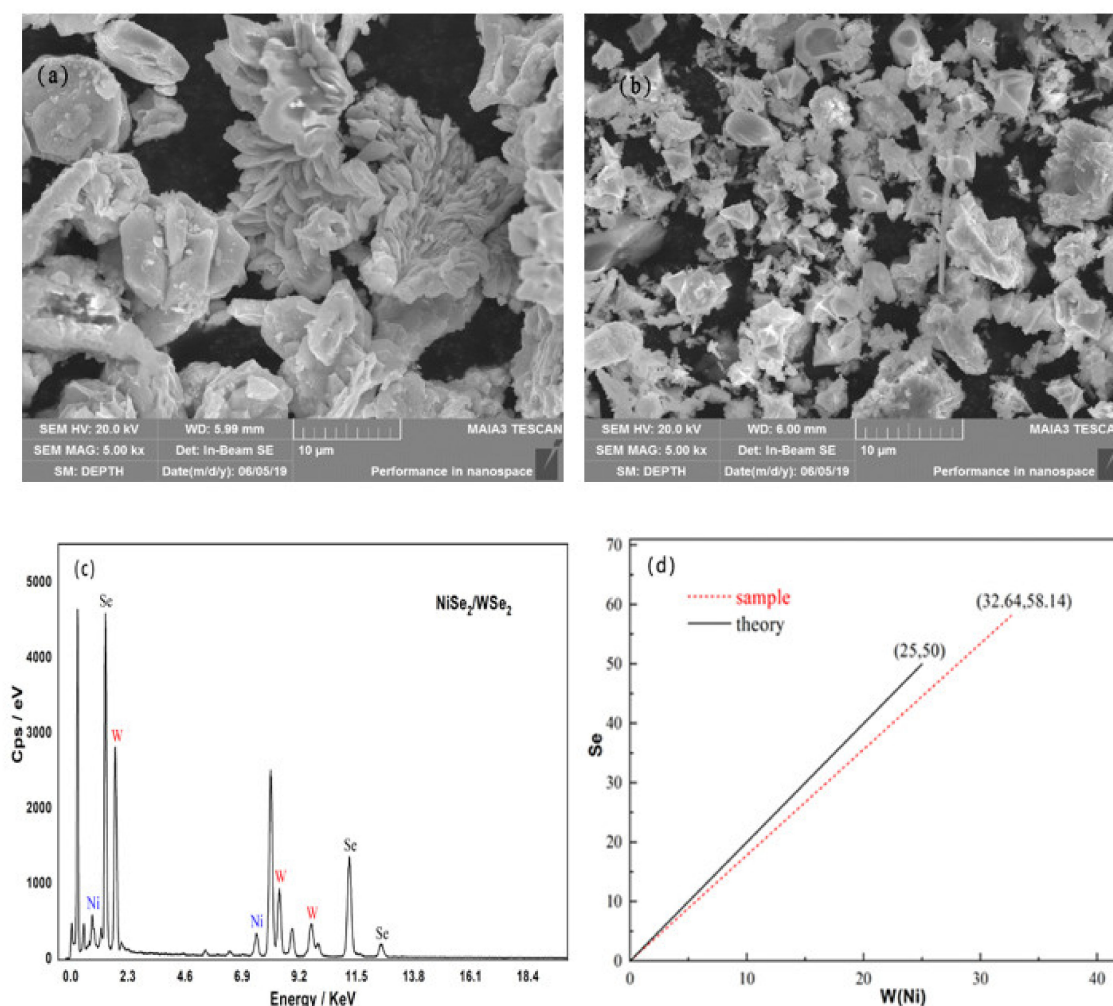


Figure 4. The full XPS spectra of (a)  $\text{NiSe}_2/\text{WSe}_2$ , (b) high-resolution XPS spectra of  $\text{Ni}2p$ , (c)  $\text{Se}3d$ , (d)  $\text{W}4f$ .

### 3.2. SEM Analysis

Figure 5a,b show the SEM images of  $WSe_2$  and  $NiSe_2/WSe_2$ , respectively. From Figure 5a, it can be seen that the  $WSe_2$  morphology presents the flower shape stacked by many flakes; in Figure 5b, the hexagonal material is  $NiSe_2$ ; after being synthesized with  $NiSe_2$ , the morphology of  $WSe_2$  changes from stacked flakes to smaller and more trivial crystal flakes, which have richer exposed edges and can provide more active sites to contact the  $CO_2$  in the reaction solution. In the meantime, the specific surface area is also increased, which is consistent with the results of BET analysis, and this benefits the adsorption of  $CO_2$ . Furthermore, from these images, it can be seen that  $NiSe_2$  and  $WSe_2$  present a homogeneous distribution and great dispersibility, which has not only solved the tendency for aggregation of  $WSe_2$  but the conductivity of material is also increased, so as to achieve the objective of improving the catalysis performance and stability of  $NiSe_2/WSe_2$ . The EDS image of  $NiSe_2/WSe_2$  is shown in Figure 5c. The Se/W atomic ratio of the sample is shown in Figure 5d. The X-axis represents the W atom percentage, the Y-axis represents the percentage of Se atom, and the slope represents the Se/W atomic ratio. The Se/W (Ni) = 1.78 in the  $NiSe_2/WSe_2$  sample. Figure 5d corresponds to the theoretical value of Se / W (Ni) (theoretical value is 2), which further proves that the sample is the target product.



**Figure 5.** SEM of (a)  $WSe_2$ ; (b)  $NiSe_2/WSe_2$ ; (c) EDS of  $NiSe_2/WSe_2$ ; (d) Atom ratio of  $NiSe_2/WSe_2$ .

### 3.3. BET Analysis

Figure 6 shows the adsorption–desorption isothermal diagram of  $N_2$ . According to Figure 6, the adsorption isothermal diagram of  $WSe_2$  and the desorption isothermal diagram of  $NiSe_2/WSe_2$  form a hysteresis loop without overlapping, which presents type IV isotherm with hysteresis loop. In other words, after synthesizing with  $NiSe_2$ , the isothermal diagram of  $NiSe_2/WSe_2$  is still type IV, which indicates that the introduction of  $NiSe_2$  has damaged the mesoporous structure of the material. Figure 6 exhibits the pore diameter distribution curve. According to Figure 7, it could be seen that the pore diameter of  $WSe_2$  and  $NiSe_2/WSe_2$  are mainly distributed in the range of 2–10 nm, but  $NiSe_2/WSe_2$  still contains very few large pores, which is mainly caused by the distribution of  $NiSe_2$ .

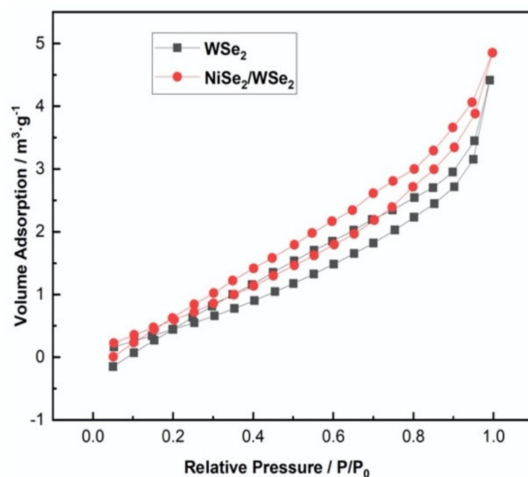


Figure 6. Adsorption–desorption curve of  $N_2$ .

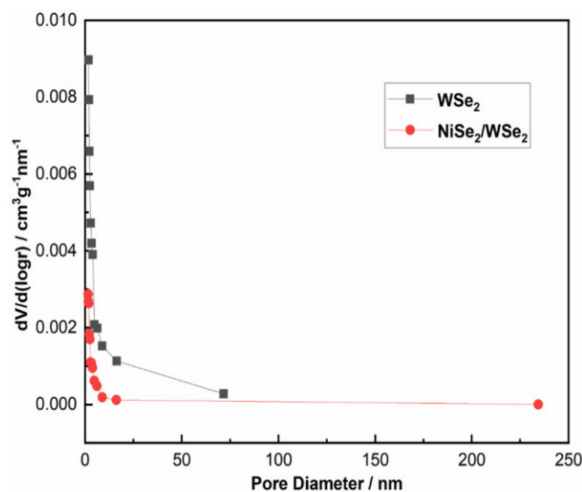


Figure 7. Pore diameter distribution curve.

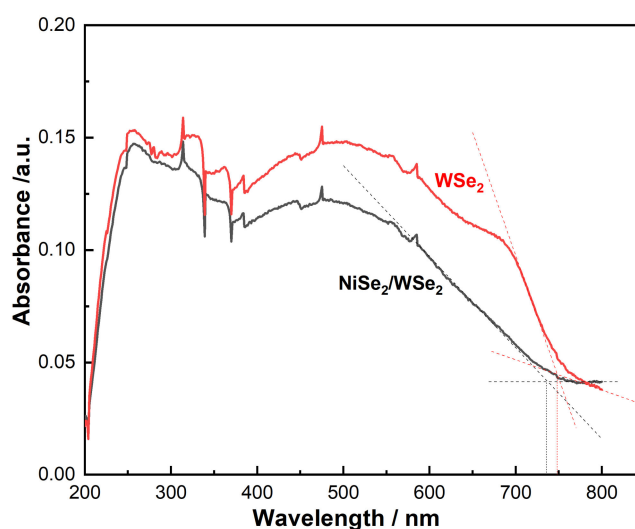
Table 1 shows the specific surface area, pore volume, and pore diameter of  $WSe_2$  and  $NiSe_2/WSe_2$ . According to Table 1, the specific surface area of  $NiSe_2/WSe_2$  presents a significant increase compared to that of pure  $WSe_2$ , which has increased by 1.83 times. This indicates the increase of active sites on the surface of  $NiSe_2/WSe_2$ , which can benefit the adsorption of  $CO_2$  and the exchange of  $CO_2$  in the pore passage. Its macroscopic expression is the high activity of the catalyst, so that the photocatalysis performance can be further improved.

**Table 1.** Specific surface area, pore volume, and pore diameter of WSe<sub>2</sub> and NiSe<sub>2</sub>/WSe<sub>2</sub>.

Sample	Specific Surface Area (m <sup>2</sup> ·g <sup>-1</sup> )	Pore Volumes (cc·g <sup>-1</sup> )	Average Pore Diameter (nm)
WSe <sub>2</sub>	3.007	0.007	1.702
NiSe <sub>2</sub> /WSe <sub>2</sub>	8.522	0.008	1.916

### 3.4. Analysis of UV-Visible Absorbance Spectrum

When WSe<sub>2</sub> is a bulk material, it is a 1.2 eV indirect band gap semiconductor, while the direct band gap for single-layer WSe<sub>2</sub> is 1.6–1.7 eV. According to Figure 8, it can be seen that WSe<sub>2</sub> and NiSe<sub>2</sub>/WSe<sub>2</sub> both show a strong photo response within the range of 250–750 nm. Although they demonstrate different light absorption intensities at different wavelengths, within the wavelength range of 250–750 nm, WSe<sub>2</sub> and NiSe<sub>2</sub>/WSe<sub>2</sub> show basically the same variation trend of light absorption intensities, which means that the introduction of NiSe<sub>2</sub> has not changed the light absorption performance of WSe<sub>2</sub>. The intersection line plotting method is employed to plot the absorption wavelength threshold in Figure 8, and it can be obtained that  $\lambda_{WSe_2} = 748$  nm,  $\lambda_{NiSe_2/WSe_2} = 736$  nm. By combining formula  $E = h * c/\lambda$ , the band gap widths of WSe<sub>2</sub> and NiSe<sub>2</sub>/WSe<sub>2</sub> can be obtained, which are 1.66 eV and 1.68 eV, respectively, indicating that the synthesized WSe<sub>2</sub> has a single layer. It has been learnt that because of the combined effects of Ni doping, which in turn cause the increase of energy of the surrounding electronics and the Burstein–Moss effect, the band gap after doping is increased so that the band gap of NiSe<sub>2</sub>/WSe<sub>2</sub> is the larger one. Note that such an increase contributes to the separation of photo-generated electrons and photo-generated holes and reduces the recombination rate of electron–hole pairs; therefore, the effective number of photo-generated electrons and photo-generated holes is increased. The goal of improving photocatalytic performance can be thereby fulfilled.

**Figure 8.** UV-visible absorbance spectrum.

### 3.5. Photocatalysis Performance

Figure 9 shows the relationship between the yield of CH<sub>3</sub>OH obtained from the photocatalytic reduction of CO<sub>2</sub> using WSe<sub>2</sub> and NiSe<sub>2</sub>/WSe<sub>2</sub> with the time. The comparisons of CH<sub>3</sub>OH yields between the work and literatures were shown Table S1. According to Figure 9, with the increase of catalysis time, the yields of CH<sub>3</sub>OH all show an increasing trend when different catalysts are used. However, under the catalytic action of NiSe<sub>2</sub>/WSe<sub>2</sub>, the yield of methanol is significantly higher than that under the catalysis of WSe<sub>2</sub>. During the first 8 h of reaction, the overall yield of methanol shows continuous growth. However, from 8 h to 10 h of reaction, the yield of methanol basically remains the same under the catalysis of WSe<sub>2</sub>, while under the catalytic action of NiSe<sub>2</sub>/WSe<sub>2</sub>, the yield of methanol still exhibits continuous growth, increasing from 3.00 mmol g<sup>-1</sup> to 3.80 mmol g<sup>-1</sup>. This is

mainly because NiSe<sub>2</sub> and WSe<sub>2</sub> have a homogeneous distribution in NiSe<sub>2</sub>/WSe<sub>2</sub>, so that NiSe<sub>2</sub>/WSe<sub>2</sub> becomes more dispersed and will not easily aggregate. The conductivity of NiSe<sub>2</sub>/WSe<sub>2</sub>, therefore, is increased by the combination of these two materials. Its morphology is presented as the smaller and more trivial crystal flakes, the surface area therefore has been increased, and there are more active sites, all of which can help to improve its photocatalysis performance.

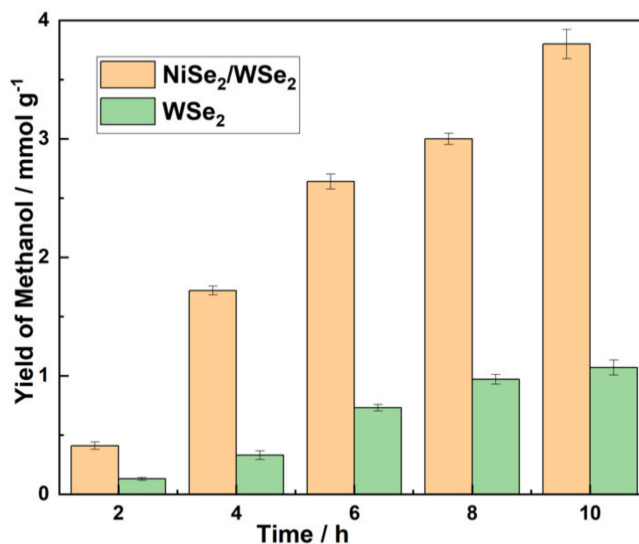


Figure 9. Relationship between the yield of methanol and the reaction time.

#### 4. Conclusions

In this paper, the hydrothermal method is employed to prepare NiSe<sub>2</sub>/WSe<sub>2</sub>. The main diffraction peak of synthesized NiSe<sub>2</sub>/WSe<sub>2</sub> is sharp, and the positions of diffraction peaks basically coincide with the standard cards of WSe<sub>2</sub> (JCPDS card, PDF#38–1388) and NiSe<sub>2</sub> (JCPDS card, PDF#41–11495); both WSe<sub>2</sub> and the synthesized NiSe<sub>2</sub>/WSe<sub>2</sub> demonstrate a strong photo response within the range of 250–750 nm, and the presence of an impurity band and band tail with the introduction of NiSe<sub>2</sub> causes the band gap of NiSe<sub>2</sub>/WSe<sub>2</sub> to become wider, from 1.66 eV to 1.68 eV, which is helpful for increasing of the effective number of photo-generated electrons and photo-generated holes. In the prepared NiSe<sub>2</sub>/WSe<sub>2</sub>, NiSe<sub>2</sub> and WSe<sub>2</sub> have a homogeneous distribution, and NiSe<sub>2</sub> also makes WSe<sub>2</sub> more dispersed; the morphology characterization changes from stacked flower shape to smaller and more trivial crystal flakes, the surface area is increased, and more active sites are provided. The photocatalytic reduction results of CO<sub>2</sub> show that the yield of CH<sub>3</sub>OH is significantly increased: the yield reaches 3.80 mmol g<sup>-1</sup> at 10 h of reaction, which is 3.4 times the yield under the catalysis of pure WSe<sub>2</sub>, and the NiSe<sub>2</sub>/WSe<sub>2</sub> has great photocatalytic activity.

#### 5. Patents

The results studied in this paper have been accepted for a patent in China with the application number 202010247325.5 and named as *A photocatalytic carbon dioxide reduction catalyst and its preparation method and application*.

**Supplementary Materials:** The following are available online at <http://www.mdpi.com/1996-1073/13/17/4330/s1>, Figure S1: XRD of synthesized WSe<sub>2</sub>, Figure S2: XPS of synthesized WSe<sub>2</sub>, Table S1: Comparison of the methanol production between this research and other literatures.

**Author Contributions:** F.G. gave the main idea regarding preparation of NiSe<sub>2</sub>/WSe<sub>2</sub> and wrote the manuscript; K.Z., Y.Z., and Y.S. prepared the NiSe<sub>2</sub>/WSe<sub>2</sub>; Z.L. and Y.L. conducted the XPS, XRD, SEM, and SEM analysis.; Z.L., Y.Z., and Y.L. performed the photocatalytic carbon dioxide reduction experiment. Z.L. and Y.L. helped in preparing the manuscript. K.L. and W.J. supervised the whole work and funding acquisition. All authors have read and agreed to the published version of the manuscript.

**Funding:** This Project is funded by the Key Research and Development (R&D) Projects of Shanxi Province, China, grant number 201803D121035.

**Conflicts of Interest:** The authors declare no conflict of interest.

## References

1. Zhao, S.; Jin, R.; Jin, R. Opportunities and Challenges in CO<sub>2</sub> Reduction by Gold- and Silver-Based Electrocatalysts: From Bulk Metals to Nanoparticles and Atomically Precise Nanoclusters. *ACS Energy Lett.* **2018**, *3*, 452–462. [[CrossRef](#)]
2. Wan, W.; Tackett, B.M.; Chen, J.G. Reactions of water and C1 molecules on carbide and metal-modified carbide surfaces. *Chem. Soc. Rev.* **2017**, *46*, 1807–1823. [[CrossRef](#)] [[PubMed](#)]
3. Koyama, S.; Akbay, E.A.; Li, Y.Y.; Herter-Sprie, G.S.; Buczkowski, K.A.; Richards, W.G.; Gandhi, L.; Redig, A.J.; Rodig, S.J.; Asahina, H.; et al. Adaptive resistance to therapeutic PD-1 blockade is associated with upregulation of alternative immune checkpoints. *Nat. Commun.* **2016**, *7*, 10501. [[CrossRef](#)] [[PubMed](#)]
4. Graves, C.; Ebbesen, S.D.; Mogensen, M.; Lackner, K.S. Sustainable hydrocarbon fuels by recycling CO<sub>2</sub> and H<sub>2</sub>O with renewable or nuclear energy. *Renew. Sustain. Energy Rev.* **2011**, *15*, 1–23. [[CrossRef](#)]
5. Stolarczyk, J.K.; Bhattacharyya, S.; Polavarapu, L.; Feldmann, J. Challenges and Prospects in Solar Water Splitting and CO<sub>2</sub> Reduction with Inorganic and Hybrid Nanostructures. *ACS Catal.* **2018**, *8*, 3602–3635. [[CrossRef](#)]
6. Wang, P.; Wang, S.; Wang, H.; Wu, Z.; Wang, L. Recent Progress on Photo-Electrocatalytic Reduction of Carbon Dioxide. *Part. Part. Syst. Charact.* **2018**, *35*, 1700371. [[CrossRef](#)]
7. Eklund, P.; Kerdsonpanya, S.; Alling, B. Transition-metal-nitride-based thin films as novel energy harvesting materials. *J. Mater. Chem. C* **2016**, *4*, 3905–3914. [[CrossRef](#)]
8. Xiao, Y.; Hwang, J.-Y.; Sun, Y.-K. Transition metal carbide-based materials: Synthesis and applications in electrochemical energy storage. *J. Mater. Chem. A* **2016**, *4*, 10379–10393. [[CrossRef](#)]
9. Asadi, M.; Kim, K.; Liu, C.; Addepalli, A.V.; Abbasi, P.; Yasaei, P.; Phillips, P.; Behranginia, A.; Cerrato, J.M.; Haasch, R.; et al. Nanostructured transition metal dichalcogenide electrocatalysts for CO<sub>2</sub> reduction in ionic liquid. *Science* **2016**, *353*, 467–470. [[CrossRef](#)]
10. Chhowalla, M.; Shin, H.S.; Eda, G.; Li, L.-J.; Loh, K.P.; Zhang, H. The chemistry of two-dimensional layered transition metal dichalcogenide nanosheets. *Nat. Chem.* **2013**, *5*, 263–275. [[CrossRef](#)]
11. Tan, C.; Zhang, H. Two-dimensional transition metal dichalcogenide nanosheet-based composites. *Chem. Soc. Rev.* **2015**, *44*, 2713–2731. [[CrossRef](#)] [[PubMed](#)]
12. Tang, H.; Dou, K.; Kaun, C.-C.; Kuang, Q.; Yang, S. MoSe<sub>2</sub> nanosheets and their graphene hybrids: Synthesis, characterization and hydrogen evolution reaction studies. *J. Mater. Chem. A* **2014**, *2*, 360–364. [[CrossRef](#)]
13. Bi, E.; Chen, H.; Yang, X.; Ye, F.; Yin, M.; Han, L. Fullerene-Structured MoSe<sub>2</sub> Hollow Spheres Anchored on Highly Nitrogen-Doped Graphene as a Conductive Catalyst for Photovoltaic Applications. *Sci. Rep.* **2015**, *5*, 13214. [[CrossRef](#)] [[PubMed](#)]
14. Fang, H.; Chuang, S.; Chang, T.C.; Takei, K.; Takahashi, T.; Javey, A. High-Performance Single Layered WSe<sub>2</sub> p-FETs with Chemically Doped Contacts. *Nano Lett.* **2012**, *12*, 3788–3792. [[CrossRef](#)] [[PubMed](#)]
15. Liu, W.; Kang, J.; Sarkar, D.; Khatami, Y.; Jena, D.; Banerjee, K. Role of Metal Contacts in Designing High-Performance Monolayer n-Type WSe<sub>2</sub> Field Effect Transistors. *Nano Lett.* **2013**, *13*, 1983–1990. [[CrossRef](#)] [[PubMed](#)]
16. Teo, W.Z.; Chng, E.L.K.; Sofer, Z. Cytotoxicity of Exfoliated Transition-Metal Dichalcogenides (MoS<sub>2</sub>, WS<sub>2</sub>, and WSe<sub>2</sub>) is Lower Than That of Graphene and its Analogues. *Chem. Eur. J.* **2014**, *20*, 9627–9632. [[CrossRef](#)]
17. Wang, H.; Feng, H.; Li, J. Graphene and Graphene-like Layered Transition Metal Dichalcogenides in Energy Conversion and Storage. *Small* **2014**, *10*, 2165–2181. [[CrossRef](#)]
18. Yu, B.; Zheng, B.; Wang, X.; Qi, F.; He, J.; Zhang, W.; Chen, Y. Enhanced photocatalytic properties of graphene modified few-layered WSe<sub>2</sub> nanosheets. *Appl. Surf. Sci.* **2017**, *400*, 420–425. [[CrossRef](#)]
19. Wang, X.; Chen, Y.; Zheng, B.; Qi, F.; He, J.; Yu, B.; Zhang, W. Significant enhancement of photocatalytic activity of multi-walled carbon nanotubes modified WSe<sub>2</sub> composite. *Mater. Lett.* **2017**, *197*, 67–70. [[CrossRef](#)]
20. Licht, S.; Myung, N.; Tenne, R.; Hodes, G. Cation Electrolytic Modification of n-WSe<sub>2</sub>/Aqueous Polyiodide Photoelectrochemistry. *J. Electrochem. Soc.* **1995**, *142*, 840. [[CrossRef](#)]

21. Feng, J.; Sun, X.; Wu, C.; Peng, L.; Lin, C.; Hu, S.; Yang, J.; Xie, Y. Metallic Few-Layered VS<sub>2</sub> Ultrathin Nanosheets: High Two-Dimensional Conductivity for In-Plane Supercapacitors. *J. Am. Chem. Soc.* **2011**, *133*, 17832–17838. [CrossRef]
22. Li, W.; Yu, B.; Hu, Y.; Wang, X.; Yang, D.; Chen, Y. Core-Shell Structure of NiSe<sub>2</sub> Nanoparticles@Nitrogen-Doped Graphene for Hydrogen Evolution Reaction in Both Acidic and Alkaline Media. *ACS Sustain. Chem. Eng.* **2019**, *7*, 4351–4359. [CrossRef]
23. Guo, J.; Shi, Y.; Bai, X.; Wang, X.; Ma, T. Atomically thin MoSe<sub>2</sub>/graphene and WSe<sub>2</sub>/graphene nanosheets for the highly efficient oxygen reduction reaction. *J. Mater. Chem. A* **2015**, *3*, 24397–24404. [CrossRef]
24. Prabhu, P.; Vishal, J.; Lee, J.M. Heterostructured Catalysts for Electrocatalytic and Photocatalytic Carbon Dioxide Reduction. *Adv. Funct. Mater.* **2020**, *30*, 24. [CrossRef]
25. Yang, X.; Yang, W.; Xin, X.; Yin, X. Enhancement of photocatalytic activity in reducing CO<sub>2</sub> over CdS/g-C<sub>3</sub>N<sub>4</sub> composite catalysts under UV light irradiation. *Chem. Phys. Lett.* **2016**, *651*, 127. [CrossRef]
26. Yu, W.; Xu, D.; Peng, T. Enhanced photocatalytic activity of g-C<sub>3</sub>N<sub>4</sub> for selective CO<sub>2</sub> reduction to CH<sub>3</sub>OH via facile coupling of ZnO: A direct Z-scheme mechanism. *J. Mater. Chem. A* **2015**, *3*, 19936. [CrossRef]
27. Bafaqeer, A.; Tahir, M. Well-designed 2D/2D ZnV<sub>2</sub>O<sub>6</sub>/g-C<sub>3</sub>N<sub>4</sub> nanosheets heterojunction with faster charges separation via pCN as mediator towards enhanced photocatalytic reduction of CO<sub>2</sub> to fuels. *Appl. Catal. B* **2019**, *242*, 312–326. [CrossRef]
28. Li, X.; Liu, H.; Luo, D.; Li, J.; Huang, Y.; Li, H.; Fang, Y.; Xu, Y.-H.; Zhu, L. Adsorption of CO<sub>2</sub> on heterostructure CdS(Bi<sub>2</sub>S<sub>3</sub>)/TiO<sub>2</sub> nanotube photocatalysts and their photocatalytic activities in the reduction of CO<sub>2</sub> to methanol under visible light irradiation. *Chem. Eng. J.* **2012**, *180*, 151. [CrossRef]
29. Qin, S.; Xin, F.; Liu, Y.; Yin, X.; Ma, W. Photocatalytic reduction of CO<sub>2</sub> in methanol to methyl formate over CuO–TiO<sub>2</sub> composite catalysts. *Chem. Eng.* **2011**, *356*, 257. [CrossRef] [PubMed]
30. Cardoso, J.C.; Stulp, S.; de Brito, J.F.; Flor, J.B.S.; Frem, R.C.G.; Zanoni, M.V.B. MOFs based on ZIF-8 deposited on TiO<sub>2</sub> nanotubes increase the surface adsorption of CO<sub>2</sub> and its photoelectrocatalytic reduction to alcohols in aqueous media. *Appl. Catal. B Environ.* **2018**, *225*, 563–573. [CrossRef]
31. Cao, K.S. Preparation and Tribological Properties of WSe<sub>2</sub> and WSe<sub>2</sub>/C Nanostructured Materials. Master's Thesis, Jiangsu University, Jiangsu, China, 2011.
32. Cho, S.; Park, S.-K.; Jeon, K.M.; Piao, Y.; Kang, Y.C. Mesoporous reduced graphene oxide/WSe<sub>2</sub> composite particles for efficient sodium-ion batteries and hydrogen evolution reactions. *Appl. Sur. Sci.* **2018**, *459*, 309–317. [CrossRef]
33. Ge, P.; Li, S.; Xu, L.; Zou, K.; Gao, X.; Cao, X.; Zou, G.; Hou, H.; Ji, X. Hierarchical Hollow-Microsphere Metal–Selenide@Carbon Composites with Rational Surface Engineering for Advanced Sodium Storage. *Adv. Energy Mater.* **2019**, *9*, 1803035. [CrossRef]
34. Gu, C.; Hu, S.; Zheng, X.; Gao, M.-R.; Zheng, Y.-R.; Shi, L.; Gao, Q.; Zheng, X.; Chu, W.; Yao, H.-B.; et al. Synthesis of Sub-2 nm Iron-Doped NiSe<sub>2</sub> Nanowires and Their Surface-Confined Oxidation for Oxygen Evolution Catalysis. *Angew. Chem. Int.* **2018**, *57*, 4084–4088. [CrossRef]

